Composites: Part B 40 (2009) 337–348

Contents lists available at ScienceDirect

Composites: Part B

journal homepage: www.elsevier.com/locate/compositesb

Size effect on strength of laminate-foam sandwich plates: Finite element analysis with interface fracture

Ferhun C. Caner [a,*], Zdeněk P. Bažant [b]

[a] Institute of Energy Technologies (INTE), School of Industrial Engineering (ETSEIB-UPC), Diagonal 647, E-08028 Barcelona, Spain
[b] Civil Engineering and Materials Science, Northwestern University, 2145 Sheridan Road, CEE/A135, Evanston, IL 60208, USA

ARTICLE INFO

Article history:
Received 31 March 2009
Accepted 31 March 2009
Available online 5 April 2009

Keywords:
Size effect
A. Sandwich plate
B. Interface fracture
A. Polymer composite

ABSTRACT

Recent three-point bend tests of size effect on the strength of geometrically scaled sandwich beams of three types – with no notches, and with notches at the upper or lower skin–foam interface, which were previously evaluated using simplified sandwich beam theory and equivalent linear elastic fracture mechanics, are now reanalyzed more accurately by finite elements. Zero-thickness interface elements with a softening cohesive law are used to model fractures at the skin–foam interface, in the fiber composite skins, and in the foam. The fracture energy and fracture process zone length of a shear crack in foam near the interface are deduced by fitting an analytical expression for size effect to the test data. Numerical simulations reveal that small-size specimens with notches just under the top skin develop plastic zones in the foam core near the edges of the loading platen, and that small-size specimens with notches just above the bottom skin develop distributed quasibrittle fracture in the foam core under tension. Both phenomena, though, are found to reduce the maximum load by less than 6%. Further it is shown that, in notch-less beams, the interface shear fracture is coupled with compression crushing of the fiber–polymer composite skin. For small specimens this mechanism is important because, when it is blocked in simulations, the maximum load increases. The size effect law for notch-less beams is calibrated such that beams of all sizes fail solely by interface shear fracture.

© 2009 Elsevier Ltd. All rights reserved.

1. Introduction

According to the current design practice, the strength of sandwich structures is determined by means of plastic limit analysis or elastic analysis with a strength limit [1,38,20,23,25,22]. This practice ignores fracture mechanics and misses the deterministic size effect. However, recent experiments at Northwestern University demonstrate that sandwich components, such as the fiber–polymer composites [29,30,35,26] and polymeric foams [8], usually fail in a brittle manner and exhibit strong deterministic size effect. Obviously, the same must be expected for sandwich plates. This is particularly important for large sandwich structures such as the hulls, decks, bulkheads, masts and antenna covers of large ships, as well as for load-bearing fuselage panels, vertical stabilizers, rudders and wing boxes of aircraft.

The type and intensity of size effect depend on the failure mechanism, i.e., different failure mechanisms require different size effect laws. Thus, in testing for size effect, it is desirable that the specimens of all sizes fail exhibit the same failure mechanism. Laminate-foam sandwich plates can fail in a variety of modes, including [14]: (1) the debonding shear fracture of skins (or face sheets), (2) fracture in the foam core, (3) compression fracture of skins [9], (4) delamination followed by skin buckling, (5) skin buckling or wrinkling [19] followed by delamination [3], and (6) foam core indentation. These modes often interact. The first three modes must, in principle, lead to deterministic size effects, and so must, at least partly, the fourth and fifth. Recent experiments reported in [6] were designed so as to obtain failure in one or both of the first two modes, although compression fracture of skins accompanied some of the failures.

Some previous studies treated skin debonding in terms of linear elastic fracture mechanics (LEFM) [36,37]. However, LEFM implies that the fracture process zone (FPZ) size shrinks to a point and the behavior is brittle. Recent size effect experiments on fiber–polymer laminates and on PVC foam, conducted at Northwestern University [7,8] reveal that the size effect is weaker than the power-law size effect of LEFM, implying quasibrittle behavior in which the FPZ size cannot be neglected. A numerical demonstration of size effect in sandwich plates with a limited size range, failing by core indentation, was reported in [10]. In that study, a simple constitutive law with softening (derived from pore collapse) was considered for the core, while the skin was assumed to have a plastic strength limit. Recently, a more comprehensive investigation of the size effect in sandwich plates, both experimental and analytical, was undertaken [6].

* Corresponding author.
E-mail addresses: ferhun.caner@upc.edu (F.C. Caner), z-bazant@northwestern.edu (Z.P. Bažant).

1359-8368/$ - see front matter © 2009 Elsevier Ltd. All rights reserved.
doi:10.1016/j.compositesb.2009.03.005

This study is focussed on sandwich plates made up of composite laminate skins and PVC foam core, which are used in the construction of various structural parts of ships and aircraft. The objectives are three: (i) to determine the shear fracture energy of the polymeric foam, (ii) to find out whether interface fracture was the only failure mechanism in Series I and II specimens that were used in [6] to validate the size effect laws; and (iii) to identify, for the cases with multiple failure mechanisms, the size effect law that corresponds to interface fracture alone. To this end, accurate finite element analyses of the test specimens are performed to fit the experimental data. Zero-thickness interface elements are inserted along the experimentally observed fracture surfaces. A cohesive fracturing law for opening and shear is used to describe the behavior of the foam core, and localized compression-shear crushing of the fiber–polymer composite skins is also taken into account.

First, a brief description of the size effect tests of the sandwich beams will be given. Following the description of the finite element analyses performed, the size effect laws for notched and notch-less sandwich plates will be formulated. Finally the results will be discussed and conclusions will be drawn. The details of the experiments analyzed [6] are summarized in the Appendix.

2. Size effect tests of sandwich beams

As reported in [6], three series of beams geometrically scaled in two dimensions were fabricated and tested in three-point bending: Series I, with beams notched symmetrically from both ends in the foam next to the interface of bottom skin (or facing, face sheet); Series II. ditto but top skin; and Series III. ditto but un-notched (Fig. 1(a)–(c)). The failure mechanism was different in each series. The scaling ratios were 1:4:16 for series I, and 1:3:9 for series II and III. The cores of sandwich beams were made of closed cell polyvinylchloride (PVC) foam, and the skins were made of woven glass-epoxy composite (FS-12A) in series I and of unidirectional carbon-epoxy composite (IM6-G/3501-6) in series II and III. For test details; see the Appendix and [6].

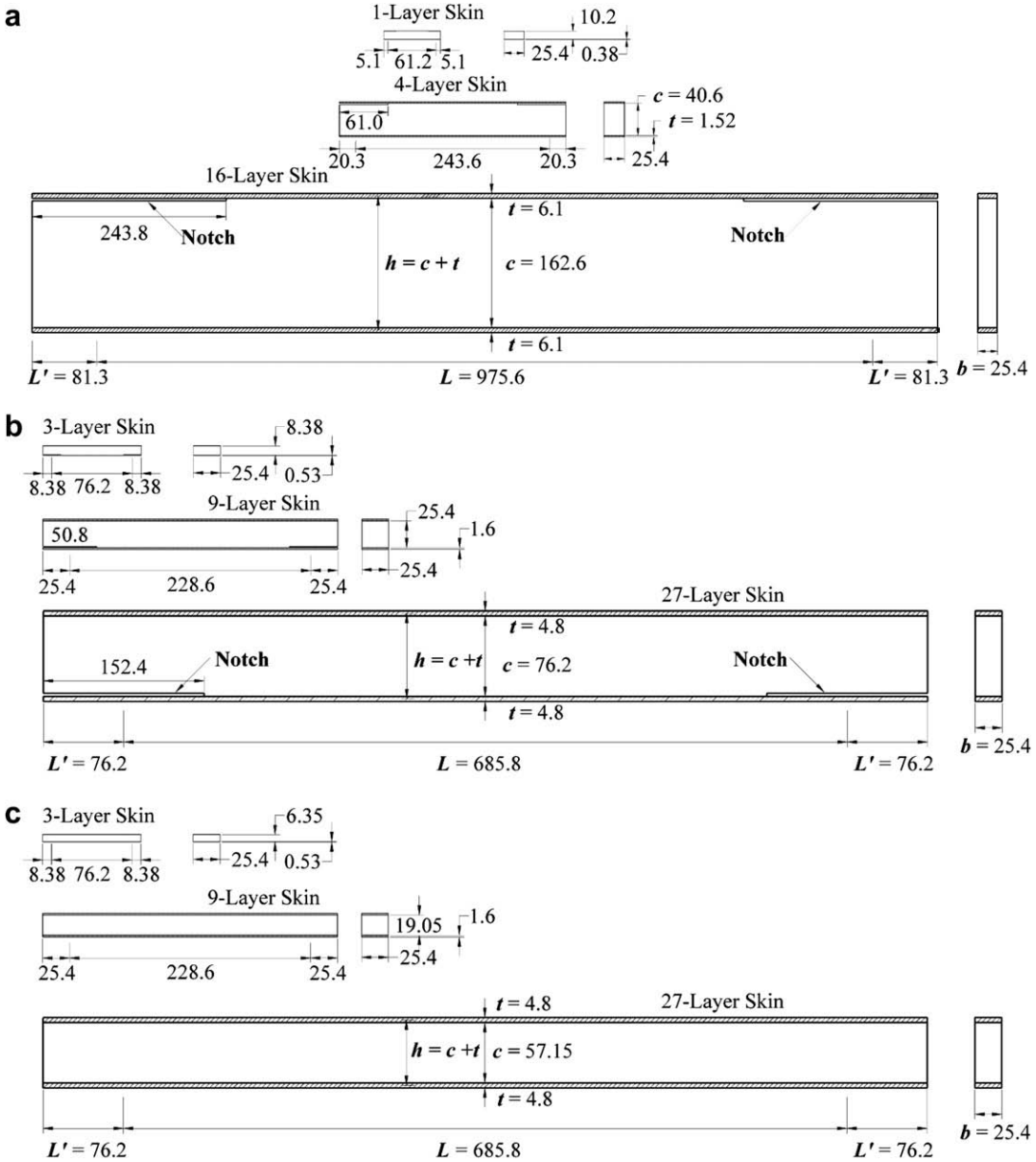

Fig. 1. Dimensions of test beams with (a) notches at top interface, (b) notches at bottom interface and (c) no notches.

The purpose of making the notches was to clarify the effect of large pre-existing cracks or damage zones, and to force the fracture to develop at a certain pre-determined location, homologous (i.e., geometrically similar) for all the sizes. Forcing the cracks to start at a predetermined location eliminates the possibility of Weibull-type statistical contribution to the size effect [2,4], because the initiating fracture cannot sample locations of different random material strength. In that case, the only effect of material randomness is a size-independent scatter of structural strength.

3. Finite element analysis of sandwich beams

3.1. The zero-thickness interface element

Cohesive shear fracture at the skin–foam interface dominated the failure in Series I and II, and was the only important failure mechanism in Series III. For finite element analysis of such failures, the so-called 'zero-thickness' interface element is a natural candidate. This element was originally introduced [21] to analyze jointed rocks. It was also employed to represent cracks in concrete [13], delamination of polymer composites [17], fracture in particle-reinforced composites [32] and biological bones [12]. Similar formulations for the so-called 'spring elements' were also developed [33,34]. In [16], a cohesive finite element, more efficient than the traditional continuum cohesive elements, was developed. For a more detailed literature review on interface elements, see [28].

This study uses an interface element that was coded (at UPC) in an implicit finite element program. The element is made up of two four-node quadrilaterals, which connect the faces of two adjacent hexahedral continuum elements. The surfaces of the two quadrilaterals are initially coincident, which means that initially the element has zero thickness. Later, these surfaces are allowed to separate, to simulate crack opening, and their relative normal and shear displacements produce normal and shear stresses, captured at Gauss points of finite elements according to the prescribed constitutive law. In three dimensions, the interface element has 24 global degrees of freedom given by the column vector $\hat{\boldsymbol{u}} = (\hat{u}_{Ii})$ where the index I varies from 1 to 8 and the index i varies from 1 to 3. The hats label the quantities at the nodes, and the corresponding quantities without hat are those defined over the element; the nodal quantities are defined with respect to global coordinates unless otherwise is noted. The nodal relative displacement vector $\Delta\hat{\boldsymbol{u}}$ is computed as the difference in displacements between the corresponding nodes [32]:

$$\Delta\hat{\boldsymbol{u}} = (\boldsymbol{I}_{12\times12} \quad -\boldsymbol{I}_{12\times12})\hat{\boldsymbol{u}} \tag{1}$$

Here $\boldsymbol{I}$ is the identity matrix; $\Delta\hat{\boldsymbol{u}} = (\Delta\hat{u}_{Ii})$ where $I = 1,2,\ldots 4$ and for each I, $i = 1,2,3$. The relative displacement field over the element can be interpolated as

$$\Delta\boldsymbol{u}(\xi,\eta) = (\phi_1\boldsymbol{I}_{3\times3}, \phi_2\boldsymbol{I}_{3\times3}, \phi_3\boldsymbol{I}_{3\times3}, \phi_4\boldsymbol{I}_{3\times3})\Delta\hat{\boldsymbol{u}} \tag{2}$$

where $\phi_I = \phi_I(\xi,\eta)$ in which $I = 1,2,\ldots 4$ are the usual shape functions; and ξ and η are the parent coordinates.

When large displacements are considered, the local coordinates $\hat{\boldsymbol{x}}_{ref}$ of the interface element may conveniently be defined as the coordinates of the midsurface between the two faces of the element [32]:

$$\hat{\boldsymbol{x}}_{ref} = \frac{1}{2}(\boldsymbol{I}_{12\times12}, \boldsymbol{I}_{12\times12})(\hat{\boldsymbol{x}} + \hat{\boldsymbol{u}}) \tag{3}$$

where $\hat{\boldsymbol{x}} = (\hat{x}_{Ii})$ are the nodal coordinates ($I = 1,2,\ldots,8$; and for each $I, i = 1,2,3$); $\hat{\boldsymbol{x}}_{ref} = (\hat{x}_{Ii}^{ref})$ where $I = 1,2,\ldots 4$; and for each $I, i = 1,2,3$. The coordinates of the midsurface could be interpolated using

$$\boldsymbol{x}_{ref}(\xi,\eta) = (\phi_1\boldsymbol{I}_{3\times3}, \phi_2\boldsymbol{I}_{3\times3}, \phi_3\boldsymbol{I}_{3\times3}, \phi_4\boldsymbol{I}_{3\times3})\hat{\boldsymbol{x}}_{ref} \tag{4}$$

When the deformations are small, the reference surface defined above becomes indistinguishable from the original surface. Next, a local coordinate system can be defined over this midsurface using the vectors:

$$\begin{aligned}\boldsymbol{t}_\xi &= \frac{\partial\boldsymbol{x}_{ref}}{\partial\xi}\frac{1}{|\partial\boldsymbol{x}_{ref}/\partial\xi|}\\ \boldsymbol{t}_\eta &= \frac{\partial\boldsymbol{x}_{ref}}{\partial\eta}\frac{1}{|\partial\boldsymbol{x}_{ref}/\partial\eta|}\\ \boldsymbol{n} &= \boldsymbol{t}_\xi \times \boldsymbol{t}_\eta\end{aligned} \tag{5}$$

The rotation matrix that transforms vectors from the global coordinate system to the local one is given by

$$\boldsymbol{R} = \begin{bmatrix} \leftarrow \boldsymbol{n} \rightarrow \\ \leftarrow \boldsymbol{t}_\xi \rightarrow \\ \leftarrow \boldsymbol{t}_\eta \rightarrow \end{bmatrix}^T \tag{6}$$

where $\leftarrow\!\!\rightarrow$ marks row vectors.

From the internal virtual work of an element,

$$\delta W_{int} = \delta\hat{\boldsymbol{u}}^T\hat{\boldsymbol{f}}^e_{int} = \int_{\partial\Omega_e}\delta\Delta\boldsymbol{u}^T\boldsymbol{t}\,\mathrm{d}S = \int_{\partial\Omega_e}(\boldsymbol{\Phi}\delta\hat{\boldsymbol{u}})^T\boldsymbol{t}\,\mathrm{d}S \tag{7}$$

one obtains the nodal forces of the element:

$$\hat{\boldsymbol{f}}^e_{int} = \int_{\partial\Omega_e}\boldsymbol{\Phi}^T\boldsymbol{t}\,\mathrm{d}S = \int_{-1}^{1}\int_{-1}^{1}\boldsymbol{\Phi}^T\boldsymbol{R}^T\boldsymbol{t}_{loc}J\,\mathrm{d}\xi\,\mathrm{d}\eta \approx \sum_g \omega\boldsymbol{\Phi}^T\boldsymbol{R}^T\boldsymbol{t}_{loc}J \tag{8}$$

where g is the Gauss point index, ω is the integration weight, $\boldsymbol{\Phi}$ is a properly arranged matrix of the shape functions ϕ_I (I = node index), $\boldsymbol{R}$ is the matrix of rotation from the global to the local coordinate systems, $\Delta\boldsymbol{t}_{loc} = \boldsymbol{C}_{loc}\boldsymbol{R}\boldsymbol{\Phi}\Delta\hat{\boldsymbol{u}}$ is the local traction vector increment, which is related to the increment of local displacement difference through a constitutive law, $\boldsymbol{C}_{loc} = \partial\boldsymbol{t}_{loc}/\partial\Delta\boldsymbol{u}_{loc}$, and J is the Jacobian of the transformation from the physical to the parent coordinates of the element.

The element stiffness matrix could be obtained using

$$\begin{aligned}\boldsymbol{K}^e_{int} &= \frac{\partial\hat{\boldsymbol{f}}^e_{int}}{\partial\hat{\boldsymbol{u}}} = \int_{\partial\Omega_e}\boldsymbol{\Phi}^T\frac{\partial\boldsymbol{t}}{\partial\Delta\boldsymbol{u}}\boldsymbol{\Phi}\mathrm{d}S = \int_{-1}^{1}\int_{-1}^{1}\boldsymbol{\Phi}^T\boldsymbol{R}^T\boldsymbol{C}_{loc}\boldsymbol{R}\boldsymbol{\Phi}J\,\mathrm{d}\xi\,\mathrm{d}\eta\\ &\approx \sum_g \omega\boldsymbol{\Phi}^T\boldsymbol{R}^T\boldsymbol{C}_{loc}\boldsymbol{R}\boldsymbol{\Phi}J\end{aligned} \tag{9}$$

3.2. Cohesive fracturing law for foam core

The mechanical behavior of the foam is assumed to be quasi-brittle, i.e., the material is assumed to be linearly elastic until the material strength limit is reached, and thereafter the material is assumed to obey a cohesive fracturing law similar to that shown in Fig. 2(a) [8]. For the size effect calculations, only the part of fracture energy corresponding to the area under the initial tangent (labelled G_{fs} in that figure) is important [5]. A linear cohesive formulation with shear-tensile coupling is necessary, for the purpose of (i) capturing the skin wrinkling, which could be a failure mechanism in the small size beams due to their very thin skins; and of (ii) simulating the curved diagonal fracture through the foam core, observed in the experiments.

To this end, an effective critical stress for the opening-shear fracture may be defined Eq. (10), ([11]):

$$\sigma_{eff} = \sqrt{\beta\sigma^2 + \tau^2} \tag{10}$$

Here β is the ratio of fracture energies in shear and tension.

Note that the cracks are properly regarded as interface cracks, for which it is impossible to distinguish between modes I and II [31,27]. Because the skin-core ratio of tensile elastic moduli is high (about 300), one might think that the cracks could be approxi-

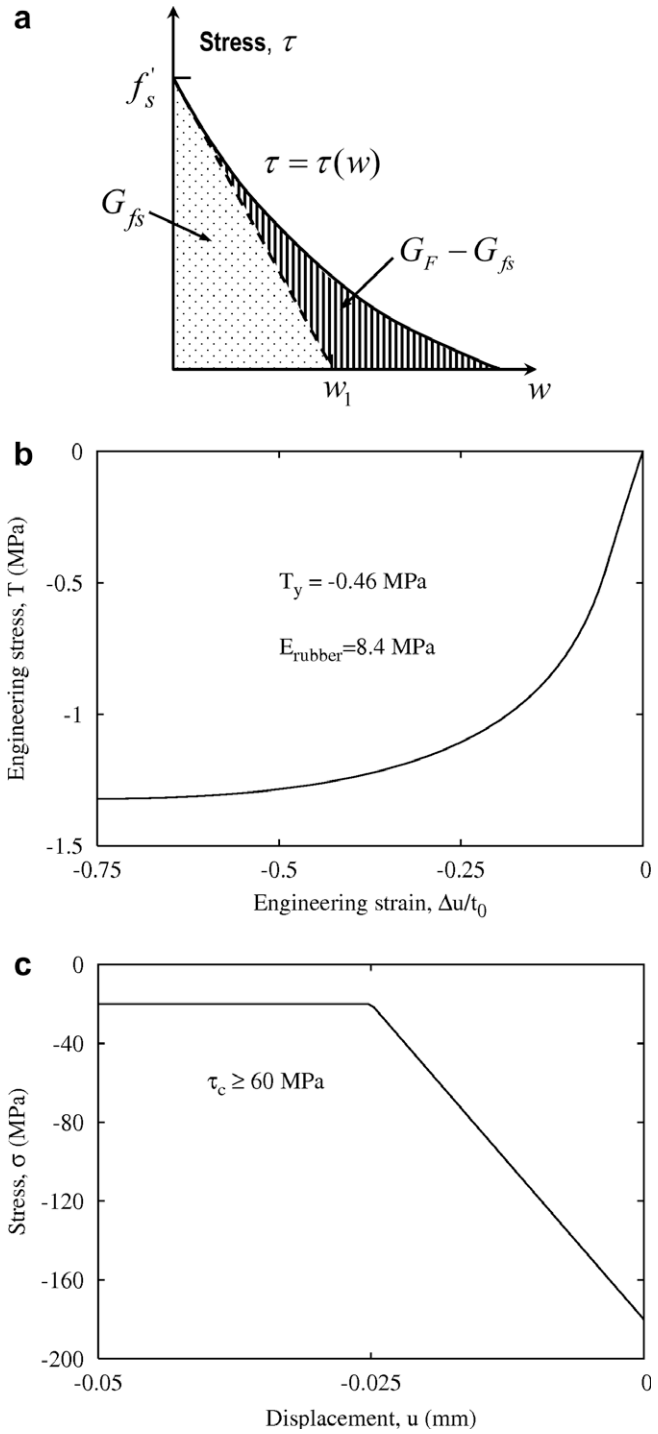

Fig. 2. The constitutive laws used in the calculations: (a) Softening cohesive stress-slip curve for shear cracks and its initial linear approximation (the numerical values for the parameters are given in the text for various cases), (b) the assumed 1D phenomenological elastic–plastic constitutive law at finite strains for the rubber sheets, and (c) softening law simulating local buckling (crushing) failure of polymer composite skin under compressive stresses triggered by shear damage in the matrix.

mately treated as delamination cracks on a rigid substrate, for which modes I and II can be distinguished. However, according to [3], the inevitable imperfections in laminate foam sandwiches always induce skin wrinkling within the FPZ, and that precludes mode separation even if the skin is much stiffer than the core.

Furthermore, it may be assumed that a potential for the cohesive stresses, $\Psi(w_{eff})$ (free energy density) exists, i.e.

$$\sigma_{eff} = \beta\sigma\frac{w_{eff}}{w^\sigma} = \tau\frac{w_{eff}}{w^\tau} \tag{11}$$

where w^σ and w^τ are the respective cohesive displacements in tension and in shear at which the corresponding cohesive stresses become zero. Substitution of Eq. 11 into Eq. 10 yields the effective cohesive displacement in terms of the cohesive displacements in tension and shear:

$$w_{eff} = \sqrt{(w^\sigma)^2/\beta + (w^\tau)^2} \tag{12}$$

Then the cohesive law may be prescribed as a relation between the effective cohesive stress and displacements, i.e., $\sigma_{eff} = \sigma_{eff}(w_{eff})$.

The evolution of both tensile stress $\sigma(w^\sigma)$ and shear stress $\tau(w^\tau)$ can be determined incrementally during the formation of opening-shear cohesive fracture $\sigma_{eff}(w_{eff})$:

$$\frac{\Delta\sigma}{\Delta\tau} = \frac{\sigma_{prev}}{\tau_{prev}} \text{ or } \frac{\Delta\sigma}{\Delta\tau} = \frac{\Delta\sigma_{prev}}{\Delta\tau_{prev}} \tag{13}$$

Here the subscript 'prev' labels the previously converged value(see Fig. 2(a), and imagine the vertical axis to be σ_{eff} and the horizontal axis to be w_{eff}). But it is found that although this formulation converges for large size beams, for small size beams it might not.

This problem may be overcome by an alternative formulation, similar to that of [11], in which separate cohesive laws are prescribed individually for tensile and shear stresses, while the tensile and shear strength values at which crack initiates are determined from the criterion

$$\sigma_{eff} = \sqrt{\beta\sigma^2 + \tau^2} = f' \tag{14}$$

Here $f' = 1.6$ MPa = initial effective stress for opening and shear. Optimal fitting of the experimental data shown in Fig. 3(a)–(c) furnished $\beta = 0.22$ and $G_{fs} = 0.40$ kN/mm. Once the crack initiates, the tensile and shear stresses are ramped down to zero, during proportional loading, from their values at fracture initiation, which are $w = w_1^\sigma = 0.28$ mm and $w = w_1^\tau = 0.5$ m. When there is pure tensile stress, then, at the initiation of cohesive fracture, $\sigma_{eff} = \sqrt{\beta}f_t' = \sqrt{\beta}3.4 = 1.6$ MPa and, with advancing fracture, the tensile stress is ramped down from 3.4 MPa to zero at $w = w_1^\sigma = 0.28$ mm. This leads to a purely tensile cohesive fracture with fracture energy $G_f = f_t' w_1^\sigma/2 = 0.49$ N/mm, which is a value reported in [8]. On the other hand, when there is only shear loading, then, at crack initiation, $\sigma_{eff} = f_s' = 1.6$ MPa, and, with advancing fracture, the shear stress is ramped down from 1.6 MPa to zero at $w = w_1^\tau = 0.5$ mm. This leads to a pure shear fracture with fracture energy $G_{fs} = f_s' w_1^\tau/2 = 0.40$ N/mm.

The softening laws for tensile and shear fractures are given by

$$\sigma^b = 1 - \frac{w^\sigma}{w_1^\sigma}\sigma_0$$
$$\tau^b = 1 - \frac{|w^\tau|}{w_1^\tau}\tau_0 \mathrm{sgn}(w^\tau) \tag{15}$$

In the foregoing equations, $w^\sigma \geqslant 0$ is the normal (opening) displacement; $w_1^\sigma = 0.28$ mm is the critical normal (opening) displacement beyond which the cohesive stress vanishes; $< x >$ is x if $x > 0$ and 0 otherwise; σ_0 and τ_0 are, respectively, the tensile stress and shear stress at which the critical stress intensity factor is reached; w^τ is the shear displacement; $w_1^\tau = 0.5$ mm is the critical shear displacement beyond which the cohesive shear stress vanishes; and $\mathrm{sgn}(x)$ is -1 if $x < 0$ and $+1$ otherwise.

Assuming unloading and reloading to be linear, one may calculate the stresses as

$$\sigma = \min\left(\frac{\sigma_{prev}^b}{w_{prev}^\sigma}w^\sigma, \sigma^b\right)$$
$$\tau = \min\left(\left|\frac{\tau_{prev}^b}{w_{prev}^\tau}w^\tau\right|, |\tau^b|\right)\mathrm{sgn}(w^\tau) \tag{16}$$

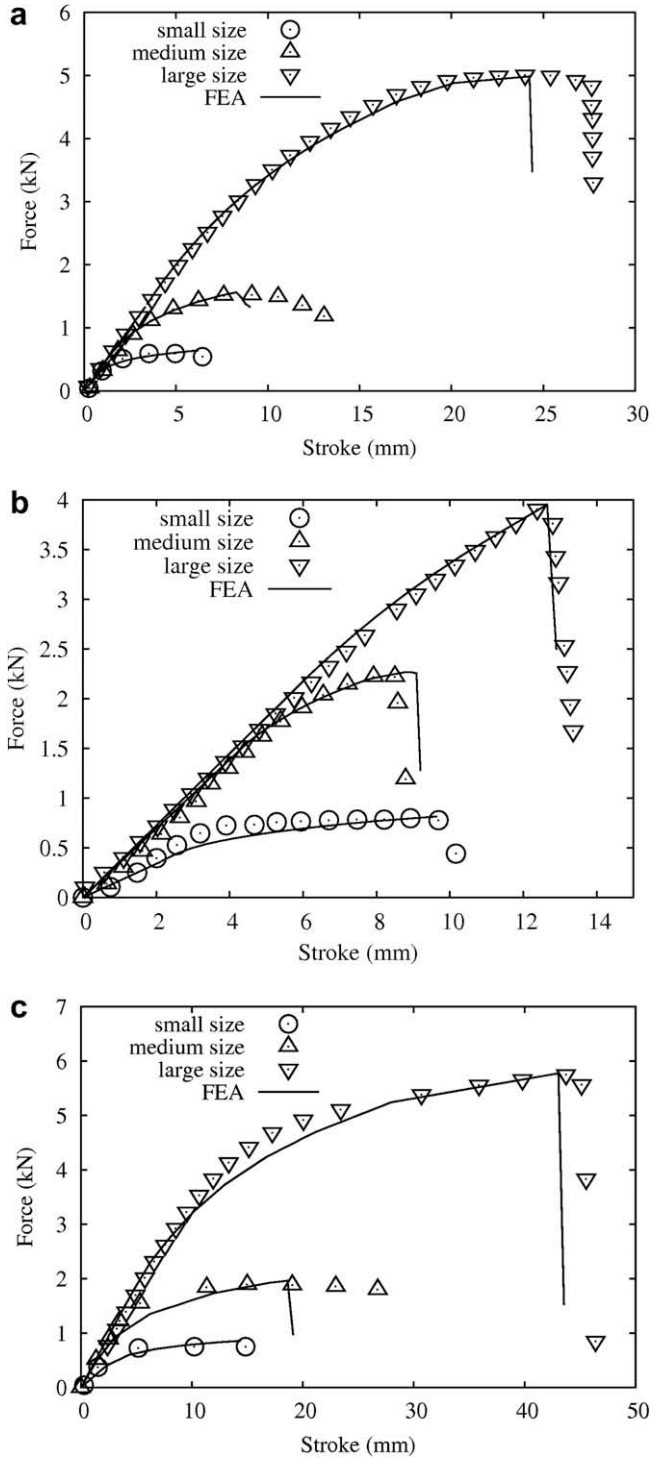

Fig. 3. Load vs load-point displacement fits of experimental data on three different sizes of (a) top-notched beams, (b) bottom-notched beams and (c) beams without notch.

where σ^b_{prev} or w^σ_{prev}, and τ^b_{prev} or w^τ_{prev} are, respectively, the latest stress or displacement indicators of tensile damage and shear damage.

Obviously, in this alternative formulation, a cohesive potential does not exist. Nevertheless, experience shows that this formulation normally converges, even under highly nonproportional loads.

To simulate cracks in the foam adjacent to the skin–foam interface, the foregoing cohesive laws are used as the constitutive relations for the interface elements. They are also used in the interface elements simulating curved cracks in the foam core, which formed in Series II and III. Taking into account the combined opening-shear fracture at the skin–foam interface is found to be indispensable for fitting the test data for all the small size specimens; otherwise the calculated response would always overestimate the data. For the medium size specimens, this is less important, and for the large size specimens it is not important at all. This finding for cohesive cracks is analogous to the fact that the near-tip field of sharp interface cracks cannot be scaled and the ratio of near-tip normal and shear stresses on the crack extension line varies when the crack length changes [31,27].

3.3. Softening laws for failure of upper composite skin

The failures of un-notched sandwich beams exhibited damage in the composite skin. The composite (IM6-G/3501-6) from which these beams were made was analyzed in [24,15], and the compressive strength of the beam was shown to depend on the shear strength of the composite along the fiber direction, and on the initial misalignment of the fibers. Thus, the damage in the skins, in the form of local crushing with fiber separation around the edges of the loading platen, must have been induced by a local shear failure of the composite skin, because local buckling of the fibers could not occur without sufficient shear damage in the matrix.

Initially, the composite skin behaves linearly, according to a transversely isotropic stiffness matrix. It is assumed that the composite fails under a local shear concentration next to the edge of the loading platen, which gives rise to the local buckling of the fibers under compression. This crushing failure of the upper skin is modelled by inserting interface elements perpendicular to the fibers.

The constitutive law for the interface elements may be written as (see Fig. 2(c)):

$$\text{if } \tau \geqslant \tau_c : \sigma^b_c = \min\left[\left(1-\frac{w^c}{w^c_1}\right)\sigma^c_0, \sigma^r_c\right]$$
$$\sigma = \max\left(\frac{\sigma^{prev}_c}{w^c_{prev}} w^c, \sigma^b_c\right) \tag{17}$$

Here $w^c < 0$ is the normal (crushing) displacement; $w^c_0 = -0.025$ mm is the critical normal (crushing) displacement beyond which the cohesive stress reduces to the residual stress $\sigma^r_c = -20$ MPa; $\sigma^c_0 = -180$ MPa = compressive stress at which the crushing is triggered; σ^{prev}_c is the latest stress indicator of crushing damage; and $\tau_c = 60$ MPa = shear strength of the composite along the fiber direction, which takes into account the fiber misalignment [24]. The residual stress, σ^r_c, is generally important only when the post-peak load-deflection curve needs to be obtained, but this is not the case here; σ^r_c may be important for size effect calculations only if crushing in the composite becomes extensive before the peak load is reached.

It is found that the crushing law just described is crucial for being able to fit the experimental data for sandwich beams without notches. For small size sandwich beams, it is necessary to assume a tensile failure criterion for failure of the upper skin because, at the edge of the loading platen, the tests show a sharp local curvature causing additional compressive and tensile stresses. As crushing of the top of the upper skin progresses, the tensile stresses at the bottom of the upper skin gradually increase and reach the tensile strength of the composite before the peak load. At that moment, however, the tensile stress drops suddenly to zero and the beam fails. Thus the composite is assumed to fail in tension, with a sudden drop of the normal stress to zero when the tensile strength is exhausted.

3.4. Simulation of notches

One possibility to simulate a notch is to mesh it as a stress-free surface. However, because the notch faces will come into contact with advancing deformations, a contact algorithm would also be needed in this case. Therefore, the notches are conveniently meshed as if they were regular interface elements. Then, the constitutive law for the interface elements in the notch zone is prescribed as

$$\tau = 0; \sigma = E_{notch} < -w^{\sigma} > \mathrm{sgn}(w^{\sigma}) \tag{18}$$

where τ and σ are, respectively, the shear and normal resistance of the interface element against sliding and opening. According to this equation, no shearing resistance is provided at the notch by the interface elements. The friction between the surfaces when they are in contact is neglected. When the normal displacements are tensile, again no resistance is generated. But if the normal displacements are compressive, then the stress becomes very large because of a large penalty parameter, $E_{notch} = 10^4$ GPa.

In the case of bottom-notched specimens, Coulomb friction effects, if needed, may be taken into account by modifying appropriately the first of the Eq. 18. However, the friction at these notches is found not to be significant enough to affect the load–displacement response.

3.5. Effect of rubber sheet under loading platen

It is well known that the compressive crushing strength of polymer composites along the fiber direction depends on the initial fiber misalignment and the shear strength of the composite along the fiber direction [24,15]. Thus, to prevent a local shear failure of polymer composite skins around the edges of the loading platen, rubber sheets were inserted between the loading platen and the tested beam. This measure was successful in preventing the local shear failure for all the specimens tested except for the notch-less beams, which exhibited shear failure at the platen edges because of being able to sustain higher loads than the notched ones.

The deflection history was conveniently recorded in terms of stroke versus applied force. It is now found that the contraction across the rubber sheets must have significantly contributed to the stroke measured in the medium and large size specimens, and so it must be taken into account. In the small size specimens, because of their lower failure load, the contribution of deformation in the rubber sheets to the total deformation recorded is negligible.

Common rubbers are known to exhibit no inelastic deformation and follow the Mooney–Rivlin elastic material model. However, comparison of the test results with the finite element simulations indicates that the rubber sheets under the loading platens in the medium and large size specimens must have behaved quasi-plastically before the peak load was reached. Although full explanation of this behavior is beyond the scope of this study, one may surmise that, under vertical compression, these sheets exhibited, due to their negligible bulk compressibility, large lateral expansions, which caused them to slip in contact with both the platens and the laminate skins. The lateral expansion due to slipping may allow the rubber sheet thickness to contract as if it were plastic (i.e., although the slip of rubber on the microscale consists of propagation of tiny ripples of separation, the resulting effect is roughly similar to a plastic deformation).

The apparent quasi-plastic behavior of the rubber sheets is represented, in the phenomenological sense, by a simple one-dimensional elastic plastic constitutive law, as shown in Fig. 2(b). To identify this law from the test data, the dimensions of the loading platen and the thickness of the sheets were considered. A linear elastic law with $E_{rubber} = 8.4$ MPa was found to suffice to fit the experimental data in the elastic range. The engineering stress at yield that, allowing the best fit of the experimental data of all the series (a total of 9 test data), is $T_y = -0.46$ MPa. Thus, the compressive constitutive law of the rubber sheets may be expressed as

$$T = E_{rubber}\Delta u/t_0 \quad \text{if} \quad 0 \geqslant \Delta u/t_0 \geqslant -0.055$$
$$T = A\ln(-\Delta u/t_0) + B(1 + \Delta u/t_0) + C \quad \text{if} \quad \Delta u/t_0 < -0.055 \tag{19}$$

where $A = -0.4943$ MPa; $B = -0.6549$ MPa; $C = -1.3$ MPa; t_0 = initial thickness of the rubber sheet, Δu = its compressive displacement, and T = engineering stress in compression.

3.6. Size effect law for unnotched sandwich beams failing by interface shear fracture

Although skin failure is one important phenomenon for sandwich structures, this study is focussed only on the cohesive shear failure at the skin–foam interface and its implications for size effect on the nominal strength of the sandwich beams. Now that we have calibrated the finite element model, we try to predict the failure loads of Series III specimens when they fail by interface shear fracture only. The finite element results for such failures are shown in Fig. 4(a) and (b).

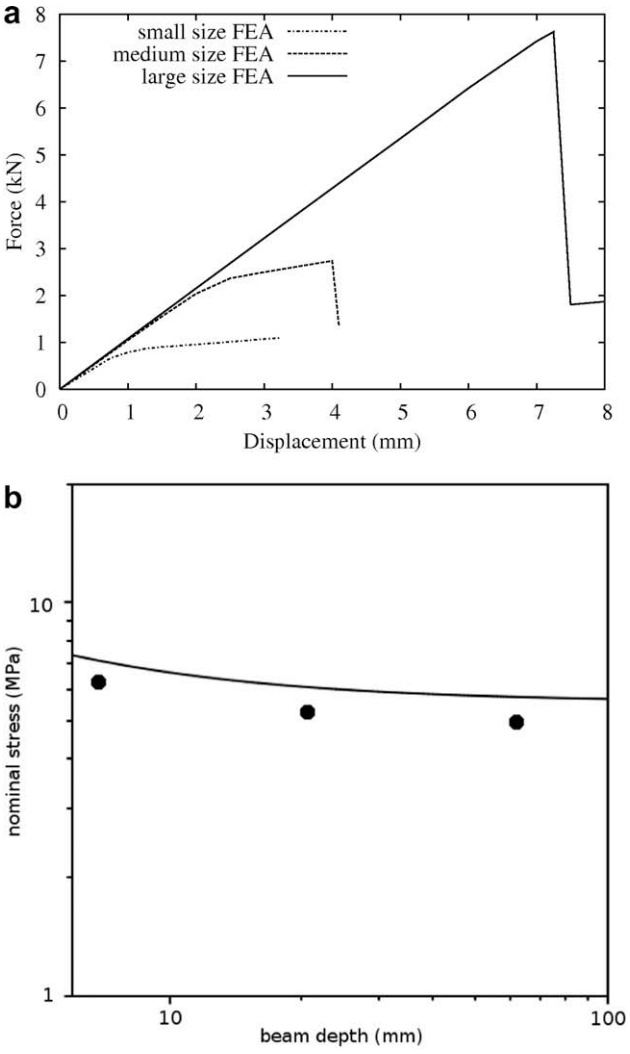

Fig. 4. (a) The force–displacement predictions of the Series III sandwich beams that fail with only interface shear fracture; displacements are free of rubber contribution, (b) predicted nominal strength of these beams and their comparison to the size effect law for failure at crack initiation given in Eq. 23.

A comparison of the predicted failure loads shown in Fig. 4(a) with the measured ones shown in Fig. 3(c) indicates that, when only the interface shear failure is considered, the failure loads are much larger than the measured ones, especially in the small size specimens. Thus, it is necessary to recalibrate the size effect law proposed in [6].

As observed in finite element calculations, the notch-less beams fail as soon as the fracture process zone (FPZ) forms at the skin–foam interface. Approximating quasibrittle fracture according to the equivalent linear elastic fracture mechanics (LEFM), one can express the nominal strength as [7,2,5]

$$\sigma_N = \sqrt{\frac{EG_{fs}}{g(\alpha)h}};\ \alpha = \frac{a}{h};\ a = a_0 + c_f \tag{20}$$

where E is Young's modulus; a_0 is the length of the stress-free crack at maximum load; a is the length of the equivalent crack at maximum load; α is the dimensionless crack length; and c_f is the half length of FPZ, which is assumed to be size independent. In the foregoing equation, $g(\alpha) = k^2(\alpha)$ where $k(\alpha) = K_I b\sqrt{h}/P$ in which K_I is the stress intensity factor; P is the failure load; and b, h are the beam width and depth. Normally $g(\alpha)$ is calculated numerically for specimens under complex boundary conditions, and analytically for simpler ones. This study uses an approximation of $g(\alpha)$ obtained in [6] analytically, based on enriched sandwich beam theory:

$$g(\alpha) = 175,200\alpha^3 - 536,200\alpha^2 + 686,600\alpha \tag{21}$$

Because failure happens as soon as the FPZ develops its full size, the first three terms of the Taylor series expansion of $g(\alpha)$ are needed (the first two terms do not suffice because the first term $g(\alpha_0) = 0$ at $\alpha_0 = 0$);

$$g(\alpha) \approx g'(\alpha_0)\frac{c_f}{h} + \frac{1}{2}g''(\alpha_0)\left(\frac{c_f}{h}\right)^2 \tag{22}$$

which is substituted into Eq. 20. Next, the resulting expression is modified so that it provides the simplest asymptotic matching of the small-size and large-size nominal stress expressions up to the first two nonzero terms; this yields [5]:

$$\sigma_N = \sigma_N^{\infty}\left(1 + \frac{h_b}{h}\right) \tag{23}$$

in which the constants $\sigma_N^{\infty} = \sqrt{EG_{fs}/(g'(0)c_f)}$ and $h_b = -c_f g''(0)/(4g'(0))$.

The optimal fit of the predicted nominal stress values is shown in Fig. 4(b). The optimal values of fracture energy and the half length of FPZ are found to be $G_{fs} = 987.4$ kN/mm and $c_f = 4.85$ mm. These values are, as expected, much larger than those obtained from the experimental failure loads of these beams, which were reported in [6] to be $G_{fs} = 240.4$ kN/mm and $c_f = 2.9$ mm.

4. Results and discussion

The finite element calculations were run up to the peak load and a little beyond, using the displacement control, under conditions identical to the experiments. In each loading step, after convergence, the principal stresses were calculated at all the Gauss points to check that the maximum tensile, maximum compressive and maximum shear stresses are not smaller than the values supplied by the manufacturer, which were 3.4 ± 1.0 MPa, 2.0 ± 0.35 MPa and 1.6 ± 0.2 MPa, respectively [18].

The dimensions of the test specimens of three different sizes of series I, which are taken from [6], are shown in Fig. 1(a). The beams in this series have notches at the top interface between the skin and the foam. The test data reported in that study and the corresponding finite element simulations obtained in this study are shown in Fig. 3(a). The fits are excellent, for specimens of all the sizes. In Fig. 5(a)–(c), the boundary conditions, the deformed configuration and the stress state at the foam–skin interface at peak load are shown for all the sizes of beams with notches at the top interface. In the simulation of series I tests, the stresses in the rubber sheet of the largest, medium and smallest specimens are found to be about 1.21 MPa, 1.03 MPa and 0.5 MPa, respectively.

The dimensions of the test specimens of three different sizes of series II, taken from [6], are shown in Fig. 1(b). The beams in this series had notches at the bottom interface between the skin and the foam. The test data reported in that study and the corresponding finite element simulations obtained in this study are shown in

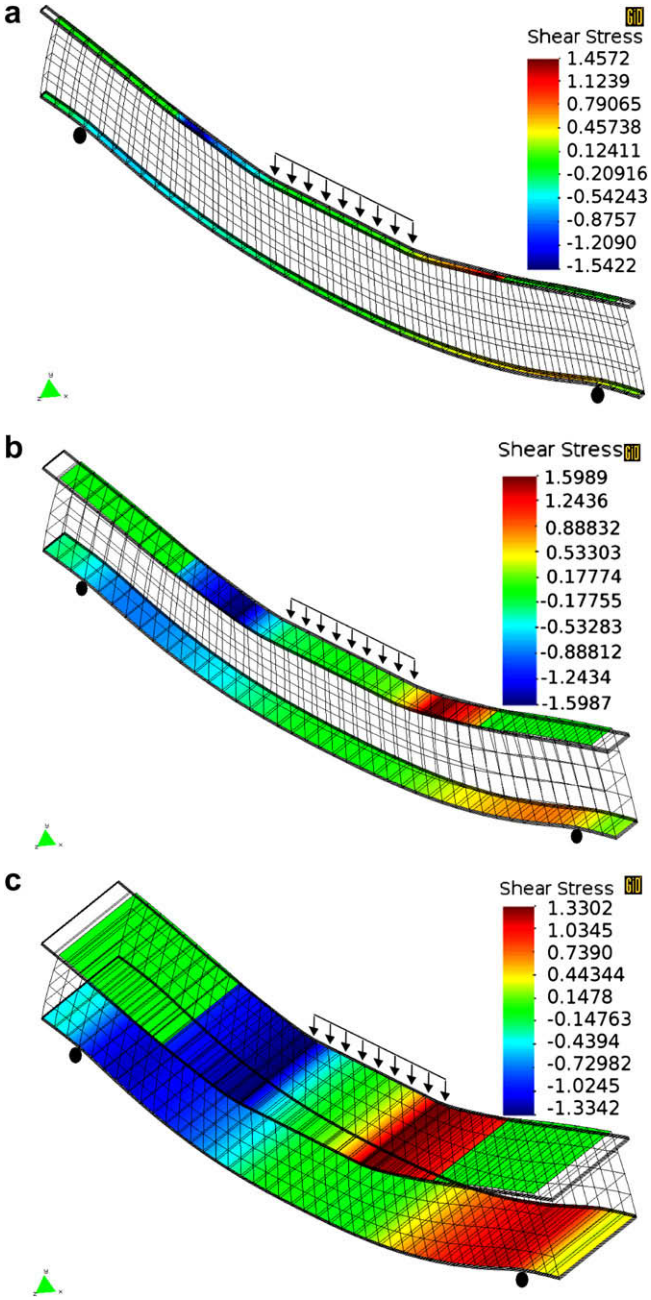

Fig. 5. (a) Oblique view of deformed mesh and shear stress distribution at the interfaces of the large size top-notched beam, (b) oblique view of deformed mesh and shear stress distribution at the interfaces of the medium size top-notched beam, (c) oblique view of deformed mesh and shear stress distribution at the interfaces of the small size top-notched beam.

Fig. 3(b). For all the sizes, the fits are excellent. In Fig. 6(a)–(c), the boundary conditions, the deformed configuration and the state of stress at both the foam–skin interface and the diagonal curved cracks at peak load are shown for all the sizes of beams with notches at bottom interface. In the simulation of series II tests, the stresses in the rubber sheet of the largest, medium and smallest specimens at maximum load are again found to be about 1.0 MPa, 1.1 MPa and 0.54 MPa, respectively.

The dimensions of the test specimens of three different sizes of series III, taken from [6], are shown in Fig. 1(c). The beams in this series had no notches. The test data reported in that study and the corresponding finite element simulations obtained in this study are shown in Fig. 3(c). The fits are again excellent for specimens of all the sizes. In the simulations, the crushing of the skins had to be taken into account in accordance with the constitutive law shown in Fig. 2(c). In addition, for the small-size specimen, tensile failure of the skins had to be considered in the form of a sudden stress drop upon reaching the tensile strength. In Fig. 7(a)–(c), the boundary conditions, the deformed configuration and the state of stress at both the foam–skin interface and the diagonal curved cracks at peak load are shown for all the specimen sizes of the beams without notch. In the simulation of series III tests, the stresses in the rubber sheet of the largest, medium and smallest specimens at maximum load were found to be about 1.3 MPa, 1.07 MPa and 0.6 MPa, respectively.

To achieve the fits shown in Fig. 3(a)–(c), it is essential to consider a combined opening-shear cohesive fracture. When the com-

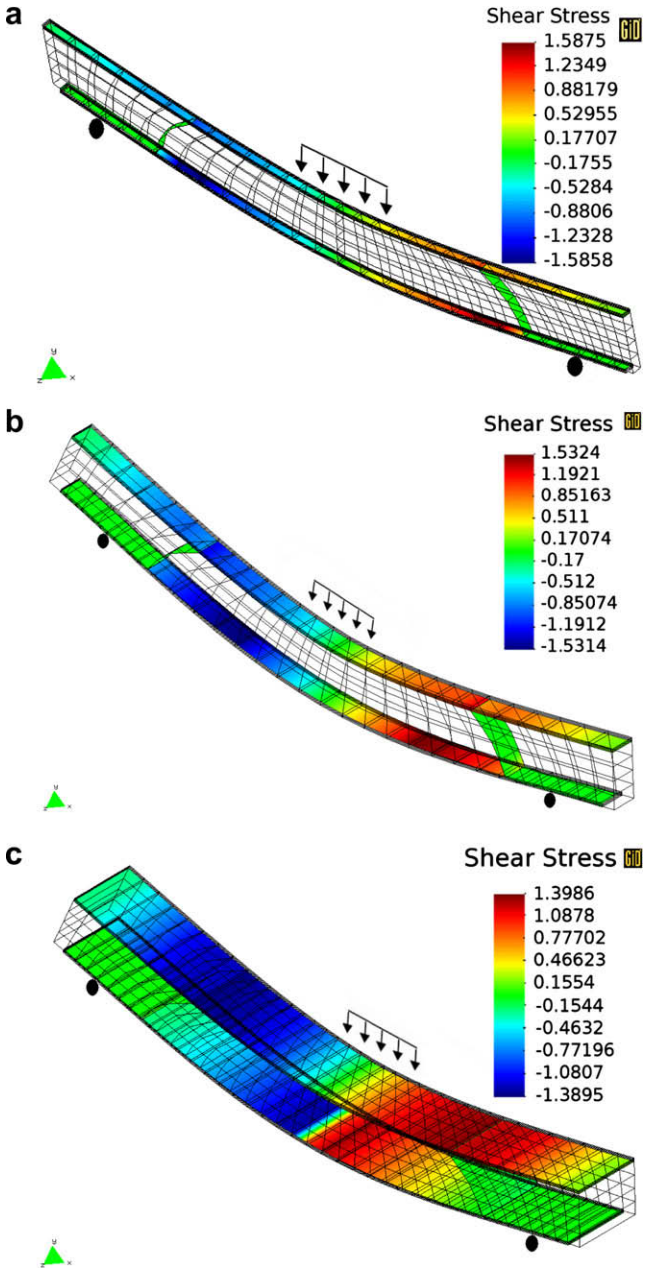

Fig. 6. (a) Oblique view of deformed mesh and shear stress distribution at the interfaces of the large size bottom-notched beam, (b) oblique view of deformed mesh and shear stress distribution at the interfaces of the medium size bottom-notched beam, (c) oblique view of deformed mesh and shear stress distribution at the interfaces of the small size bottom-notched beam.

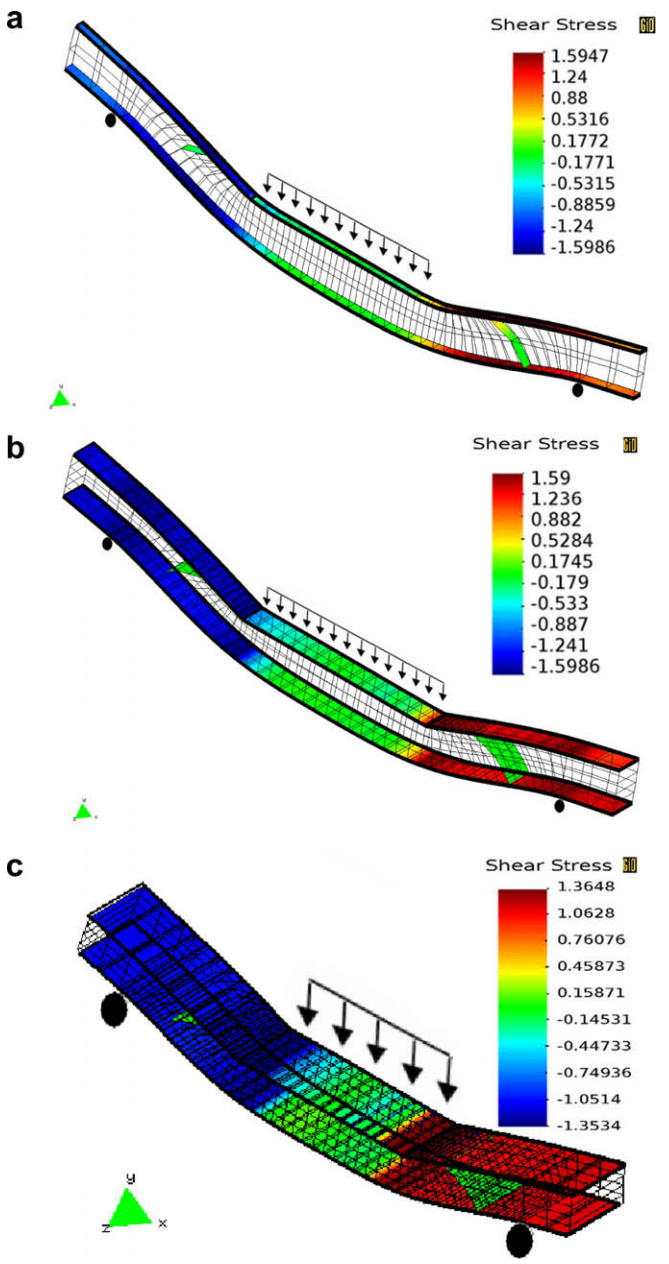

Fig. 7. (a) Oblique view of deformed mesh and shear stress distribution at the interfaces of the large size beam without notch, (b) oblique view of deformed mesh and shear stress distribution at the interfaces of the medium size beam without notch, (c) oblique view of deformed mesh and shear stress distribution at the interfaces of the small size beam without notch.

bined opening-shear nature of the fracture at the skin–foam interface is neglected, the calculated load–displacement response always overestimates the experimental data in small and medium size specimens of all the three series. The numerical simulation of the large-size specimens, on the other hand, is found capable of fitting the experimental data equally well, regardless of whether a cohesive opening-shear fracture, or a purely cohesive shear fracture, is employed. Consequently, to capture the combined opening-shear effects, it is important to use a fine mesh for small-size specimens. For large-size specimens, on the other hand, relatively coarse meshes can be employed. The meshing requirements for the medium-size specimens are in between.

According to the Figs. 5 and 7 the notched specimens develop relatively longer and longer cracks along the notched interface as the specimen size changes from large to small. Diagonal curved cracks were allowed to form in the foam core for Series II and Series III specimens, to find out whether these cracks could develop before or after the peak load. In the simulations of Series II specimens, these cracks were found to form only in the post-peak regime when the axial stresses get transferred from the skins to the foam core, due to a large reduction of interface shear resistance. By contrast, simulation of the notch-less specimens in Series III showed limited fracture propagation at the skin–foam interface.

According to the simulations of the large and medium size specimens, the interface fracture initiates at the edges of loading platens near the support, at which skin crushing takes place. For a smaller specimen size, the initiating crack spreads over a larger and larger portion of the interface, which is explained by an increasing ratio of the FPZ size to specimen size.

Note the abrupt curvature change at the crushed skins, as simulated by the interface elements inserted perpendicular to the fiber direction in the upper skins. The stress state in the diagonal curved cracks at peak load indicates that the diagonal fracture happens only after the peak load.

It is found that failure in the small-size specimens of Series I and II developed before the peak load, and only within the foam core and the interface. In all the larger specimens of Series I and II, the beams are found to have failed by interface shear fracture only, which is manifested by quasibrittle behavior. However, the additional failure mechanisms vary among the small-size specimens from one series to the other. Fig. 8(a) and (b) depict the minimum and maximum principal stress distributions, respectively. Under uniaxial compression, the pore collapse in foam is known to be energetically more favorable than the shear failure [8]. Thus, in the small-size specimens of top-notched beams, pore collapse in the foam core took place, after a large interface fracture, near the edges of the loading platen, as shown in Fig. 8(a). In the bottom-notched small-size specimens, again after the growth of very long interface fracture, distributed tensile cracks are found to have formed in the bottom half of the foam core, as shown in Fig. 8(b).

When the additional failure mechanisms are blocked in the simulations, the maximum increase in the peak load of the top-notched and bottom-notched small size specimens is found to be less than 6% and 11% respectively. Thus, the effect of this change on the size effect law proposed for top-notched and bottom-notched specimens in [6] must be small.

In the simulations of notch-less beams, it is found that the additional failure mechanism that must have intervened in all the beams is the failure of skin. Modeling of failure of the composite skin in the form of compression crushing of fibers is sufficient to achieve the peak load in the large- and medium-size specimens but, in the small-size specimen, tensile failure of the skin must be considered. Except at the two interfaces, the foam core remains elastic everywhere in all three specimens until the peak load is reached. When this additional failure mechanism is ignored, the increase in computed maximum load is relatively very large for the small-size specimens and small for the medium- and large-size specimens. Consequently, the size effect law proposed in [6] for failure at crack initiation needs to be revised.

Fig. 4(a) and (b) depict the predicted failure loads of Series III beams under interface shear fracture only, and also the size effect fit to the predicted nominal stress values. In the fit, the same function $g(\alpha)$ as determined by the enriched sandwich beam analysis [6] is used. As expected, the fracture energy and half-length of FPZ increase from $G_{fs} = 240.4\ \mathrm{kN/mm}$ and $c_f = 2.9\ \mathrm{mm}$ to $G_{fs} = 987.4\ \mathrm{kN/mm}$ and $c_f = 4.85\ \mathrm{mm}$.

One important question to answer using the present computational framework is whether the skin wrinkling is an additional failure mechanism in the small-size beams, in which the skin is very thin. To this end, it is necessary to consider an opening-shear cohesive fracture law and geometrical nonlinearity. It transpires that no skin wrinkling could have taken place in the small-size

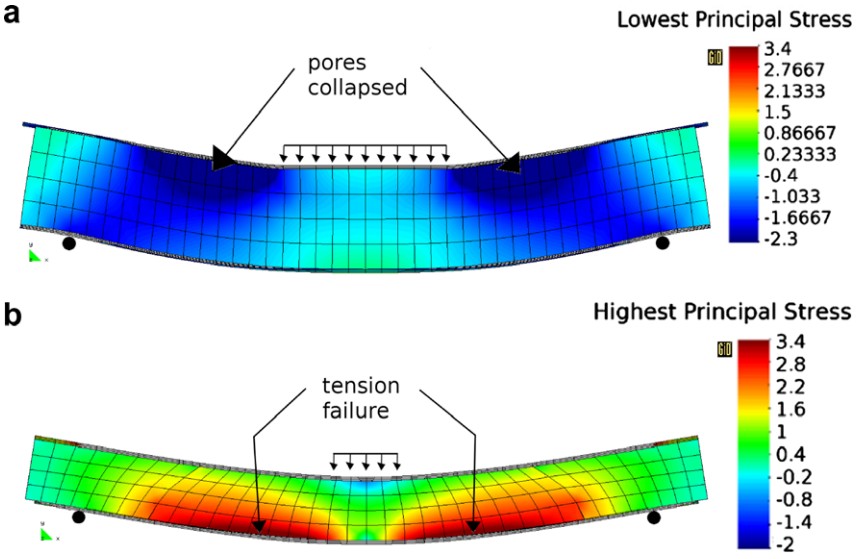

Fig. 8. (a) The pore collapse mechanism of failure of the foam core in the small size top-notched beam, (b) the distributed tension failure of foam core in the small size bottom-notched beam.

beams with notches, for three reasons: (i) The tensile strength of foam at the skin–foam interface is too high for crack initiation; (ii) once the cohesive shear fracture begins, in accordance with the combined opening-shear fracture criterion, the tensile strength at the damaged interface drops, but it drops first at the edges where the compressive stress is the smallest; and (iii) by the time the shear fracture approaches the midspan, the length of the skin subjected to high compressive stress becomes too small. Neither can skin wrinkling happen in the small-size specimens without a notch, because (i) skin crushing causes premature failure, and (ii) the bond between the foam and the skin remains too strong for any wrinkling to take place during crack initiation failure before the peak load is reached.

5. Conclusions

1. Failure of laminate-foam sandwich beams of various sizes can be realistically simulated by geometrically nonlinear finite element analysis in which cohesive cracks are represented by zero-thickness interface elements, provided that a combined cohesive opening-shear softening and skin crushing are taken into account.
2. It is important to take into account the deformation of the rubber sheets placed under the loading platens to prevent local shear failure of the laminate skin. Although rubber is perfectly elastic, the one-dimensional behavior of these rubber sheets, accounting for the effect of lateral expansion, had to be represented as elastic–plastic, in order to fit the experimental data for the medium and large size specimens. The cause of this seemingly plastic behavior under the loading platens might be the volume incompressibility of the rubber sheets and their low shear modulus, along with rippling slippage at their contact surfaces. For the smallest size beams, the effect of the deformation of rubber sheets is negligible.
3. The calculations confirm that failure of sandwich plates consisting of fiber composite skins and PVC foam core exhibits a significant size effect. This is true not only for the notched (or damaged) sandwich plates but also for the notch-less ones.
4. Consequently, it is unrealistic to predict the load capacity of large sandwich structures on the basis of material failure criteria expressed only in terms of stresses and strains, which are inherently incapable of capturing non-statistical size effects. The concepts of material strength and yield limit do not apply. Instead, the load capacity of large sandwich structures must be determined on the basis of the cohesive crack model or nonlocal continuum damage models.
5. Based on optimum fitting of failure test data, the shear fracture energy of the PVC foam is estimated to be 0.40 N/mm, which is about 82% of the opening mode fracture energy [8].
6. Aside from interface shear fracture on approach to the peak load, further failure mechanisms operate in small-size beams, but not large ones. They include compressive crushing of the foam near the edges of the loading zone in top-notched small-size beams, and distributed tensile fracture of the foam in the bottom-notched small size beams. However, these mechanisms do not have a strong effect because, when they are excluded from simulations, the increase in the computed failure load of small size beams is less than 6%.
7. The failure load of notch-less specimens is drastically affected by crushing of the skin, which can be modelled by interface elements inserted perpendicularly to fibers near the edges of the loading platen, using a compressive stress-compressive displacement law with linear softening terminating with a horizontal residual stress and triggered by the shear damage in the matrix.
8. The experimental maximum loads of notch-less beams can be closely predicted considering only shear fracture in the foam adjacent to the interface. These data show that the size effect at crack initiation is strong. By fitting the size effect law to these data, one gets, for shear fracture in the foam near the interface with skin, the FPZ half-length $c_f = 4.85$ mm, and the fracture energy $G_{fs} = 987$ kN/mm. The latter value is 2×10^6-times larger than the Mode I fracture energy of the foam material alone [8]. This may be explained by the composite action of foam and skin in which the external loads are resisted by axially very stiff skins.
9. Numerical simulations show that the curved diagonal fracture observed to run across the foam core cannot affect the peak load and thus must have formed in the post-peak regime of the tested beams.
10. Geometrically nonlinear finite element simulations with opening-shear cohesive interface fracture calibrated to fit experimental data reveal that the skin wrinkling, which might be suspected to occur in small-size beams due to their very thin skins, has not actually taken place.

Acknowledgements

Financial support from the Office of Naval Research under grants N00014-91-J-1109 and N00014-07-I-0313 to Northwestern University is gratefully acknowledged. Partial support from Grant BIA2006-12717 from MEC-Madrid is also acknowledged.

Appendix A. Summary of previous size effect tests of sandwich beams with foam core

As reported in detail in [6], the cores were made of closed cell polyvinylchloride (PVC) foam with mass density 100 kg/m^3 (25.4 mm thick sheets of Divinycell H100, procured from Diabgroup, Inc.). The properties of the foam (as specified by the supplier) were as follows [18]: tensile elastic modulus 130 ± 25 MPa, tensile strength 3.4 ± 0.4 MPa, compressive elastic modulus 135 ± 20 MPa, compressive strength 2.0 ± 0.35 MPa, elastic shear modulus 35 ± 7 MPa, and shear strength 1.6 ± 0.2 MPa. The sandwich beams fabricated had the same width, $b = 25.4$ mm, for all the three sizes (in order to eliminate any possible width effect). All of the cores were cut from the same sheet of foam [6]. The tests and finite element analyses indicated that there was a variation in the foam properties, though within the limits specified by the manufacturer. The thickness t of the skins was scaled in proportion the core depth, c.

For series I and II, notches were cut in the foam, symmetrically at both ends of beam, as close as possible to the interface with the top or bottom skin, but without cutting into the skin, and without baring it (Fig. 1(a) and (b)). The distance a of each notch tip from the support axis was equal to core depth c. Each notch tip was sharpened by a razor blade of 0.25 mm thickness.

The purpose of making the notches was to clarify the effect of large pre-existing cracks or damage zones, and to force the fracture to develop at a certain pre-determined location, homologous (geometrically similar) for all the sizes. The notches ensured the absence of statistical Weibull-type contribution to the size effect. The choice of beam and notch proportions was also guided by the need to prevent significant core indentation, which would complicate interpretation of the results. Furthermore, the notches made it possible to obtain shear fracture for a relatively small length-depth ratio of the test beams. All the beams were subjected to three-point loading.

A.1. Test series I, with fiberglass-epoxy skins and notches at top interface

According to [6], the skins of beams of series I consisted of a cured woven glass-epoxy composite (FS-12A, procured from Aerospace Composite Products, as 0.38 mm thick sheets). The following properties were obtained through material tests: longitudinal elastic modulus 30 GPa, transverse modulus 28 GPa, transverse strength 300 MPa, in-plane shear modulus 5 MPa, and in-plane shear strength 90 MPa. The depths of the foam cores were $c = 10.2,\ 40.8$ and 163.2 mm (Fig. 1(a)–(c)). The scaling of the skin thicknesses was achieved by bonding 25.4 mm wide composite strips—1 strip for the smallest beams, 4 strips for the medium beams, and 16 strips for the largest beams. The L/h ratio was 6:1 for all the beams (and thus the effective lengths of the beams were $L = 61.2,\ 244.8$ and 979.2 mm). All the beams of series I were loaded in an Instron 5000 universal testing machine.

The local failure under the corners of the loading platens is a sensitive aspect. It could be so extensive as to control the maximum load. To avoid this problem, two separate rubber sheets were placed on top of the skin. Furthermore, between these sheets and the metallic platen (aluminum for series I, and steel for series II and III), two laminate plates (consisting of the same material as the skins) were inserted (having dimensions $10 \times 25.4 \times 6$ mm, $40 \times 25.4 \times 6$ mm and $160 \times 25.4 \times 6$ mm for series I, and $17 \times 25.4 \times 4.8$ mm, $51 \times 25 \times 4.8$ mm and $154 \times 25.4 \times 4.8$ mm for series II and III). Observations during the series I tests showed that a small crack grew in the top laminate plate from the edge of the platen, but did not extend into the second laminate plate.

Fig. 3(a) shows, for all three sizes, the typical records of the load-deflection curves up to failure. They show that the larger the specimen, the more brittle its response. For example, in the largest specimen, crack propagation becomes unstable and the load suddenly drops right after the peak load, while in the smallest specimen, one can see a period of gradual post-peak softening. In the largest specimen, the loss of crack growth stability after the peak was manifested by a loud noise, while in the medium size specimen only quiet sound emissions during the gradual postpeak decline of load were heard.

A.2. Test series II, with carbon-epoxy skins and notches at bottom interface

The foam cores in series II specimens were the same as in Series I [6]. However (for no other reason than convenient availability), a different material was used for the skins—unidirectional carbon -epoxy (IM6-G/3501-6, provided by Hexcel, Inc., in a 12 inch wide roll, Young's moduli $E_1 = 172$ GPa and $E_2 = 9.5$ GPa, shear modulus $G_{12} = 5.7$ GPa and Poisson ratios $v_{12} = 0.28$ and $v_{21} = 0.02$). The prepreg material was cut into 12×12 inch sheets for the small and medium size specimens, and 34×10 in. sheets for the large specimens. Then, for small, medium and large specimens (Fig. 1(b)), respectively, 3, 9 and 27 layers of prepreg sheets were laid up. The 12×12 inch laminates were cured in a compression-lamination press (Tetrahedron MTP-14), while the 34×10 inch laminates were cured in an autoclave (McGrill). The curing process suggested by the manufacturer for the 3501-6 epoxy matrix was followed (it involved a maximum curing temperature of 350°F and a maximum curing pressure of 75 psi). After curing, the laminates were cut into $3.67 \times 1.0, 11.0 \times 1.0$ and 33.0×1.0 inch strips, by means of a diamond saw. The thicknesses of the $[0]_3$, $[0]_9$ and $[0]_{27}$ laminate skins were 0.021, 0.063 and 0.189 inch (0.53, 1.60 and 4.80 mm) for the small, medium and large specimens, respectively. The foam (Divinycell H100) was cut into $3.67 \times 0.33 \times 1.0, 11.0 \times 1.0 \times 1.0$ and $33.0 \times 3.0 \times 1.0$ inch ($93.2 \times 8.4 \times 25.4, 279.6 \times 25.4 \times 25.4$, $839.0 \times 76.2 \times 25.4$ mm) blocks for the small, medium and large specimens, respectively. The L/c ratio of these beams was 9:1, and thus the effective beam lengths were 3, 9 and 27 inch, or 76.2, 228.6 and 685.8 mm, respectively (Fig. 1(b)).

The skins and foam cores were bonded together by epoxy adhesive and were cured in a vacuum bag for 8 hours.

The small and medium specimens were tested under three-point bending in a universal testing machine (MTS, 20 kip), while the large specimens were tested in a larger machine (MTS 220 kip) because of their greater dimensions rather than strength. The loading rate was chosen so as to reach the peak load of the specimens of all the sizes within about 3 minutes [6].

For all the specimens, without exception, the final failure mode observed after the load dropped included diagonal tensile fracture which propagated through the foam [6]. Whether the diagonal tensile fracture in the foam occurred after, at, or just before the peak load was not recorded. The post-peak behavior confirmed that the larger the specimen, the greater the brittleness of response. The load-deflection curves for all three specimen sizes are shown in Fig. 3(b).

A.3. Test series III, with carbon-epoxy skins and no notches

As reported in [6], the beams of test series III were the same as in series II, except that the foam block dimensions were $3.67 \times 0.25 \times 1.0,\ 11.0 \times 0.75 \times 1.0,\ 33.0 \times 2.25 \times 1.0$ in. or $93.2 \times 6.4 \times 25.4,\ 279.6 \times 19.0 \times 25.4,\ 839.0 \times 57.2 \times 25.4$ mm, which means that the ratio of L/c was 12:1. In addition, the notches were absent (Fig. 1(c)). The scaling ratios of the length and depth dimensions of all the beams were 1:3:9 (Fig. 1(c)).

In series III, the failure modes varied. In the small beams, no diagonal shear fracture was observed and the failure was caused by compressive fracture of the upper skin. This mode of failure was also observed in some medium and large beams, but in most of these beams the interface crack branched into a diagonal tensile crack which crossed the foam core [6]. The measured load-deflection curves for the beams of all three sizes are shown by the points in Fig. 3(c).

References

[1] Allen HG. Analysis and design of sandwich panels. London: Pergamon Press; 1969.
[2] Bažant ZP. Scaling of structural strength, hermes penton science. London: Kogan Page Science; 2002.
[3] Bažant ZP, Grassl P. Size effect of cohesive delamination fracture triggered by sandwich skin wrinkling. J Appl Mech – ASME 2007;74(6):1134–41.
[4] Bažant ZP, Pang SD. Activation energy based extreme value statistics and size effect in brittle and quasibrittle fracture. J Mech Phys Solids 2007;55(1):91–131.
[5] Bažant ZP, Planas J. Fracture and size effect in concrete and other quasibrittle materials. Boca Raton and London: CRC Press; 1998.
[6] Bažant ZP, Zhou Y, Daniel IM, Caner FC, Yu Q. Size effect on strength of laminate-foam sandwich plates. J Eng Mater Tech Trans ASME 2006;128(3):366–74.
[7] Bažant ZP, Zhou Y, Novák D, Daniel IM. Size effect on flexural strength of fiber-composite laminate. J Eng Mater Technol – ASME 2004;126(1): 29–37.
[8] Bažant ZP, Zhou Y, Zi G, Daniel IM. Size effect and asymptotic matching analysis of fracture of closed-cell polymeric foam. Int J Solids Struct 2003;40:7197–217.
[9] Bayldon J, Bažant ZP, Daniel IM, Yu Q. Size effect on compressive strength of sandwich panels with fracture of woven laminate facesheet. J Eng Mater Technol – Trans ASME 2006;128(2):169–74.
[10] Brocca M, Bažant ZP, Daniel IM. Microplane model for stiff foams and finite element analysis of sandwich failure by core indentation. Int J Solids Struct 2001;38(8111–8132).
[11] Camacho GT, Ortiz M. Computational modeling of impact damage in brittle materials. Int J Solids Struct 1996;33(20–22):2899–938.
[12] Carol I, Lopez CM, Roa O. Micromechanical analysis of quasibrittle materials using fracture-based interface elements. Int J Num Meth Eng 2001;52:193–215.
[13] Carol I, Prat PC, Lopez CM. Normal/shear cracking model: application to discrete crack analysis. J Eng Mech – ASCE 1997;123(8):765–73.
[14] Daniel IM, Gdoutos EE, Wang K-A, Abot JL. Failure modes of composite sandwich beams. Int J Damage Mech 2002;11(4):309–34.

[15] Daniel IM, Hsiao HM. Is there a thickness effect on compressive strength of unnotched composite laminates? Int J Fracture 1999;95:143–58.
[16] De Xie, Waas A. Discrete cohesive zone model for mixed-mode fracture using finite element analysis. Eng Fracture Mech 2006;73:1783–96.
[17] de Borst R, Remmers JJC. Computational modelling of delamination. Compos Sci Tech 2006;66(6):713–22.
[18] A.B. Diab International. Divinycell H Technical Manual; 2006.
[19] Gdoutos EE, Daniel IM, Wang K-A, Abot JL. Nonlinear behavior of composite sandwich beams in three-point bending. Exp Mech 2001;41:182–8.
[20] Goodier JN, Neou IM. The evaluation of theoretical critical compression in sandwich plates. J Aeronaut Sci 1951;18:649–57.
[21] Goodman RE, Taylor RL, Brekke TL. A model for the mechanics of jointed rock. ASCE J Soil Mech Fdns Div 1968;99:637–59.
[22] Gough GS, Elam CF, De Bruyne ND. The stabilization of a thin sheet by continuous supporting medium. J Roy Aeronaut Soc 1940;44:12–43.
[23] Hansen U. Compression behavior of frp sandwich specimens with interface debonds. J Compos Mater 1998;32(4):335–60.
[24] Hsiao HM, Daniel IM, Cordes RD. Dynamic compressive behavior of thick composite materials. Exp Mech 1998;38(3):172–80.
[25] Hunt GW, de Silva LS. Interactive bending behavior of sandwich beams. J Appl Mech – ASME 1990;57:189–96.
[26] Hunt GW, Wadee MA. Localization and mode interaction in sandwich structures. Proc Roy Soc London A 1998;454:1197–216.
[27] Hutchinson JW, Mear ME, Rice JR. Crack paralleling an interface between dissimilar materials. J Appl Mech – ASME 1987;54:828–32.
[28] Karabatakis DA, Hatzigogos TN. Analysis of creep behavior using interface elements. Comp Geotech 2002;29:257–77.
[29] Pearce TRA, Webber JPH. Buckling of sandwich panels with laminated faceplates. Aeronaut Quart 1973;24:295–312.
[30] Plantema FJ. Sandwich construction, the bending and buckling of sandwich beams, plates and shells. New York: J. Wiley and Sons; 1966.
[31] Rice JR. Elastic fracture mechanics concepts for interface cracks. J Appl Mech – ASME 1988;55:98–103.
[32] Segurado J, Llorca J. A new three-dimensional interface finite element to simulate fracture in composites. Int J Solids Struct 2004;41:2977–93.
[33] Song SJ, Waas A. Mode I fracture in laminates. Eng Fracture Mech 1994;49(1):17–28.
[34] Song SJ, Waas A. An energy based model for mixed mode failure of laminated composites. AIAA J 1995;33(4):739–45.
[35] Triantafillou TC, Gibson LG. Failure mode maps for foam core sandwich beams. Mater Sci Eng 1987;95:37–53.
[36] Zenkert D. Strength of sandwich beams with mid-plane debondings in the core. Compos Struct 1990;15(4):279–99.
[37] Zenkert D. Strength of sandwich beams with interface debondings. Compos Struct 1991;17(4):331–50.
[38] Zenkert D, editor. The handbook of sandwich construction Engineering Materials Advisory Services (EMAS). UK: Warley; 1997.